**Guilherme R. Franzini**[1]
Department of Structural Engineering
and Geotechnics,
Escola Politécnica,
University of São Paulo–Brazil,
Av. Prof. Luciano Gualberto
travessa 3 n° 380-05508-010,
São Paulo, SP, Brazil

**Celso P. Pesce**
Offshore Mechanics Laboratory (LMO),
Escola Politécnica,
University of São Paulo–Brazil,
Av. Prof. Luciano Gualberto
travessa 3 n° 380-05508-010,
São Paulo, SP, Brazil

**Rafael Salles**
Offshore Mechanics Laboratory (LMO),
Escola Politécnica,
University of São Paulo–Brazil,
Av. Prof. Luciano Gualberto
travessa 3 n° 380-05508-010,
São Paulo, SP, Brazil

**Rodolfo T. Gonçalves**
Numerical Offshore Tank (TPN),
Escola Politécnica,
University of São Paulo–Brazil,
Av. Prof. Luciano Gualberto
travessa 3 n° 380-05508-010,
São Paulo, SP, Brazil

**André L. C. Fujarra**
Numerical Offshore Tank (TPN),
Escola Politécnica,
University of São Paulo–Brazil,
Av. Prof. Luciano Gualberto
travessa 3 n° 380-05508-010,
São Paulo, SP, Brazil

**Pedro Mendes**
Center of Research and Development,
Petrobras,
Av. Horácio Macedo,
950, 21.941-915,
Rio de Janeiro, RJ, Brazil

# Experimental Analysis of a Vertical and Flexible Cylinder in Water: Response to Top Motion Excitation and Parametric Resonance

*Experiments with a vertical, flexible, and submerged cylinder were carried out to investigate fundamental aspects of risers dynamics subjected to harmonic excitation at the top. The flexible model was designed aiming a high level of dynamic similarity with a real riser. Vertical motion, with amplitude of 1% of the unstretched length, was imposed with a device driven by a servomotor. Responses to distinct exciting frequency ratios were investigated, namely, $f_I$:$f_{N,1}$ = 1:3; 1:1; 2:1, and 3:1. Cartesian coordinates of 43 monitored points positioned all along the span were experimentally acquired by using an optical tracking system. A simple Galerkin's projection applied for modal decomposition, combined with standard Mathieu chart analysis, led to the identification of parametric resonances. A curious finding is that the Mathieu instability may simultaneously occur in more than one mode, leading to interesting dynamic behaviors, also revealed through standard power spectra analysis and displacement scalograms.* [DOI: 10.1115/1.4029265]

*Keywords: experiments, flexible cylinder, imposed top motions, Mathieu instabilities, modal analysis*

## 1 Introduction

In the offshore scenario, structural elements such as risers and tethers are subjected to highly complex nonlinear dynamic phenomena. Most of these behaviors are majorly regulated by tension, parameter that is responsible for what is commonly referred to as geometric stiffness; see, e.g., Pesce and Martins [1]. In the absence of current action, waves, and, consequently, floating unity motions, riser tension is only function of space, governed by its own weight. On the other hand, motions of the floating unities, which are concomitantly caused by first- and second-orders free surface wave forces, by current and by wind, modulate riser tension in time, within a large range of frequencies, from slow to high values.

Tension modulations are intrinsically associated to Eigen frequencies modulations, which may be a key point in the study of resonant fluid–structure interaction phenomena, such as vortex-induced vibrations (VIVs); see, for example, Silveira et al. [2], Joseffson and Dalton [3], and Srinil [4].

From the mathematical point of view, a riser subjected only to tension modulation can be modeled as a nonautonomous system, in which one parameter (geometric stiffness) is function of time. In this case, the Hill's equation governs the structural dynamics. Considering that the tension modulation is harmonic and monochromatic, a particular case of Hill's equation named Mathieu's equation is responsible for the dynamics. Deeper discussion regarding Hill's and Mathieu's equation can be found in several text books of dynamics, such as Meirovitch [5].

The most common form of Mathieu's equation is the nondamped one. However, physical systems are usually low-damped. Furthermore, within the fluid–structure interaction scope, hydrodynamic damping is usually modeled as a bilinear function of velocity, as in Morrison's equation. Ramani et al. [6] performed a

[1]Corresponding author.

Contributed by the Technical Committee on Vibration and Sound of ASME for publication in the Journal of Vibration and Acoustics. Manuscript received April 1, 2014; final manuscript received November 25, 2014; published online January 27, 2015. Assoc. Editor: Paul C.-P. Chao.

  

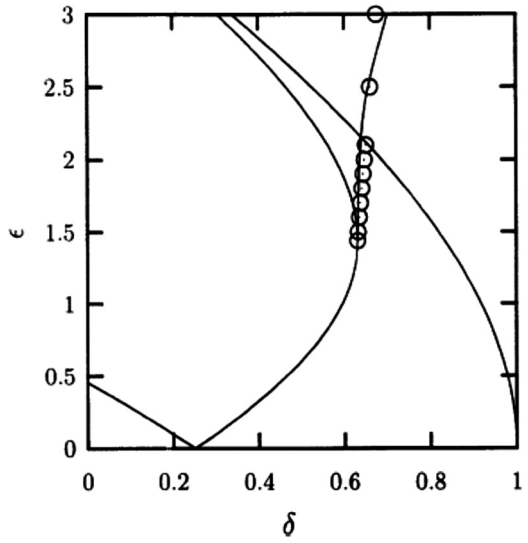


**Fig. 1 Strutt diagram obtained from Eq. (1) and the secondary bifurcation curve in the $\delta$–$\varepsilon$ plane. Focus on the first instability region. Extracted from Ref. [6].**

thorough theoretical–numerical investigation on the Mathieu equation[2] written as

$$\ddot{u} + |\dot{u}|\dot{u} + (\delta + \varepsilon \cos t)u = 0 \tag{1}$$

Consider first the nondamped case. The origin $x = 0$ is the trivial solution of the Mathieu's equation. However, depending on the combination of parameters $\bar{\delta}$ and $\bar{\varepsilon}$, this solution may be not stable. A common approach to check the instability of the origin is the so-called Strutt diagram. The Strutt diagram allows to identify regions in the plane of parameters $\bar{\delta} - \bar{\varepsilon}$ where the trivial solution (the origin) is stable or unstable. These regions are defined by transition curves (following the nomenclature adopted in Ref. [6]) which can be numerically determined solving determinantal equations presented, for example, in Ref. [5].

Focusing now the damped case, Ref. [6] presents numerical simulations and analytical considerations regarding the behavior of Eq. (1). Besides discussions on the structural bifurcation caused by the inclusion of the quadratic damping term, the authors discuss the existence of a secondary bifurcation, "in which a pair of limit cycles come together and disappear (a saddle-node of limit cycles)" [6]. This secondary bifurcation emanates from the point $\bar{\delta} \approx 0.6304$ and $\bar{\varepsilon} \approx 1.4386$, following the local analytical approximation obtained in Ref. [6], $\delta = -0.00534\varepsilon^5 + 0.04716\varepsilon^4 - 0.13696\varepsilon^3 + 0.14908\varepsilon^2 - 0.01551\varepsilon + 0.58301$. Figure 1 illustrates the Strutt diagram obtained from Eq. (1), corresponding to the various stable and unstable regions [6].

Returning to the context of dynamics of risers and tethers, Mathieu instability and other phenomena have been focus of investigations during the last decades. Patel and Park [7] pointed out that, even in the instability region of the Strutt diagram, the oscillations are limited, due to the hydrodynamic damping term. Simos and Pesce [8] show that the effects of tension variation along the length may play an important role in the dynamics of tension leg platform (TLP) tethers subjected to parametric excitation.

Chatjigeorgiou and Mavrakos [9] considered the coupling of longitudinal and transversal displacements in the mathematical model. Among other features, the authors pointed out that the coupled system leads to modifications in the Strutt diagram. The parametric excitation of a nonlinear beam model which takes into account the effects of extensibility in the lateral motion was investigated numerically in Zeng et al. [10], highlighting that the nonlinearities in the structural model are responsible for capturing the parametric excitation due to the surge motion of floating units. Yang et al. [11] discussed the effects of irregular top excitation instead of a single harmonic. The numerical simulations presented in the latter paper showed significant differences between the Strutt diagram obtained for single-frequency or multi-frequency parametric excitation.

As can be seen in this brief introduction, a large number of theoretical and numerical investigations regarding the Mathieu instability in the context of risers and tethers are available. On the other hand, experimental studies are not so common as theoretical ones. The focus of this paper is to present experimental results of a flexible and immersed cylinder subjected to harmonic top motion excitation and to discuss the Mathieu instability by plotting onto the Strutt diagram the experimental parameters obtained for the first three Eigen modes. For the sake of organization, this paper is composed by six additional sections: In Sec. 2, the experimental arrangement and methodology are briefly described. In Sec. 3, the model is experimentally characterized (in still water) in terms of Eigen frequencies and Eigen modes. Section 4 describes the modal analysis approach, followed, in the Sec. 5, by the presentation of an analytical model that will be employed aiming at plotting experimental data onto the Strutt diagram. Section 6 discusses the experimental results and Sec. 7 presents the final remarks and perspectives of future works.

## 2 Experimental Arrangement and Analysis Methodology

In laboratory tests, accounting for similarities with full scale is usually a hard task. The flexible cylinder employed in this investigation was designed aiming at reaching a high level of dynamic similarity with an 8 in. riser. The methodology used for the design of the scaled model is detailed in Rateiro et al. [12]. Such a methodology is based on the Froude number similarity, related to the referred motions of the floating unity, caused by the incoming free surface waves.

A similitude investigation pointed out a family of dimensionless parameters that regulates the dynamics of a riser, as it might be regarded in Ref. [12]; all dimensionless numbers are presented in Table 1. Using Froude similarity in a usual riser of about 250 m in length and 219 mm in diameter with a reduced scale $\lambda = 100$, it was possible to build a model which fits the dimensions of the laboratory. Unfortunately scaling a 219 mm in diameter riser would result in a 2.19 mm in diameter model. Structures with less than 10 mm in diameter are difficult to instrument, especially when optical sensors are intended to be used. Reynolds similarity is obviously not preserved, and, as pointed out in Rateiro et al. [13], "Adopting a distorted scale in diameter is usual in these circumstances, what helps increasing model Reynolds number. In fact, if $\lambda_D < \lambda$ is such a distorted scale, then $\mathrm{Re_R} = (\lambda\lambda_D)^{1/2}(\mathrm{Re_M})$. This, however, might impair similarity regarding KC number,…" Anyhow, the experimental results at model scale may be used for comparing and validating numerical models. Despite the generality of the riser modeling methodology presented in Refs. [12] and [13], a single example of an 8 in. commercial pipe was chosen to be scaled. Table 2 presents the geometrical, inertial, and stiffness properties of the model.

The model was made of a silicon tube with external diameter $D = 22.2$ mm, filled in with stainless steel microspheres. The size of the microspheres was adjusted in order to represent the scaled mass per unit length. The unstretched and stretched lengths were, respectively, $L_o = 2552$ mm and $L = 2602$ mm. The immersed length was $L_i = 2257$ mm. Both axial and bending stiffness (EA and EI) of the model were experimentally evaluated following a formulation based on large displacements, as can be found by Franzini et al. [14]. Figures 2(*a*)–2(*c*) show pictures of the

[2]Notice that this particular time scaling leads to the definition of the Mathieu parameters, $\delta$ and $\varepsilon$, such that the resulting Strutt diagram has the vertex of the first unstable region located at $\delta = 0.25$.

**Table 1 Nondimensional parameters (extracted from Ref. [12])**

| Number | Symbol | Representation |
|---|---|---|
| Froude number | $\mathrm{Fr} = \frac{\omega A}{\sqrt{gL}}$ | Dynamic motion in waves |
| Reynolds number | $\mathrm{Re} = \frac{UD}{\nu}$ | Inertial forces versus viscous forces |
| Strouhal number | $\mathrm{St} = \frac{f_s D}{U}$ | Vortex shedding frequency |
| Keulegan–Carpenter number | $\mathrm{KC} = \frac{2\pi A}{D}$ | Inertial forces versus drag forces |
| Structural damping | $\zeta = \frac{c}{c_c}$ | Linear structural damping |
| Reduced velocity | $V_R = \frac{U}{f_n D}$ | Normalized velocity in VIV |
| Reduced shedding frequency | $f_s^\star = \frac{f_s}{f_n} = S_t \frac{U}{f_n D} = S_t V_r$ | Vortex shedding normalized frequency |
| Reduced mass | $m^* = \frac{m}{m_D}$ | Riser mass versus displaced mass |
| Added mass | $a = \frac{m_a}{m}$ | Added mass versus riser mass |
| Bending stiffness | $K_f = \frac{\lambda_f}{L}$ | Bending versus geometrical stiffness |
| Axial stiffness | $K_a = \frac{\mathrm{EA}}{T}$ | Axial versus geometrical stiffness |

experimental arrangement and Fig. 3 sketches the experimental setup.

Harmonic displacements were imposed at the top by means of an in-house built 400 W servomotor device. The mentioned device can impose motion with maximum amplitude 280 mm with resolution of 50 $\mu$m. Further details regarding the servomotor device can be found by de Mello et al. [15]. The amplitude of the prescribed top motion was $A_t/L_o = 1\%$, a small value indeed, but large enough as representative of usual riser dynamics. Six values of top motion frequency were investigated, namely, $f_t{:}f_{N,1} = 1{:}3$; 1:2; 2:3; 1:1; 2:1, and 3:1, where $f_{N,1}$ is the first Eigen frequency evaluated from free decay tests carried out in still water. Due to limitations in the length of the paper, the cases 1:2 and 2:3 will not be discussed herein. The Cartesian coordinates of 43 reflexives and almost nonintrusive targets placed along the model were measured through a QUALISYS® optical tracking system. Six submerged cameras acquired the data from 38 underwater targets and two aerial cameras acquired the data from the remaining targets. The calibration quality of the optical motion capture system and its uncertainties depend on the number of cameras, the quality of the targets reflection, calibration time, and distance to targets. At the end of the calibration process, the optical motion capture system provided the standard deviation from the known measures. This value represents the measurement uncertainty. In that calibration process, such a value was around 0.1 mm, so of order $D/200$. The uncertainty of the measurement is larger than the uncertainty of the displacement imposed by the servomotor device.

**Table 2 Complementary model properties**

| Property | Value |
|---|---|
| Internal diameter | 15.8 mm |
| External diameter, $D$ | 22.2 mm |
| Unstretched length, $L_o$ | 2552 mm |
| Stretched length, $L$ | 2602 mm |
| Immersed length, $L_i$ | 2257 mm |
| Immersed weight, $\gamma$ | 7.88 N/m |
| Axial stiffness, EA | 1.2 kN |
| Bending stiffness, EI | 0.056 $\mathrm{Nm}^2$ |
| Mass ratio parameter, $m^*$ | 3.48 |
| Aspect ratio, $L_i/D$ | 102 |
| $L/D$ | 117 |
| Static tension at the top, $T_t$ | 40 N |

The model was mounted at the towing carriage of IPT (the São Paulo State Technological Research Institute). The lower end of the model was clamped to a support, rigidly fixed to the bottom of the carriage, while the upper end was clamped to a load cell, which measured the vertical component of tension. Typical vertical misalignment is close to 1% of the stretched length. All the data were acquired with sample frequency $f_{sp} = 60$ Hz, runs lasting 120 s.

Herein, $z$ represents the spanwise position, measured from the lower end of the cylinder. All the displacements are normalized with the diameter, i.e., $x^*(t) = x(t)/D$, $y^*(t) = y(t)/D$, and $z^*(t) = z(t)/D$.

Regarding analysis methodology, we focus on the presentation of amplitude scalograms $x^*(z^*, t)$, power density spectra (PSD) $S_x(z^*, f)$, and the Strutt diagrams. It is worth mentioning that, as this paper focus on the case without carriage speed, the response in the $x$ direction is expected to be similar to that obtained in the $y$ direction, except for unavoidable asymmetries in the experimental setup. Experiments with concomitant parametric excitation and towing speed were also carried out and will be discussed in future works.

## 3 Characterization

First, free decay tests driven by structural perturbations were carried out in still water. The spanwise distribution of the PSD is shown in Fig. 4, from which the following relation could be extracted for the $n$-Eigen frequency:

$$f_{N,n} = n0.84 \text{ Hz}, \quad n = 1, 2, 3 \tag{2}$$

Given that the bending stiffness is very small and the vertical flexible cylinder is long ($L/D > 100$), Bessel's functions, or even Wentzel–Kramers–Brillouin (WKB) approximate solutions, would be a proper choice for the Eigen modes (see, e.g., Refs. [16] and [17]). However, for the sake of simplicity, the Eigen

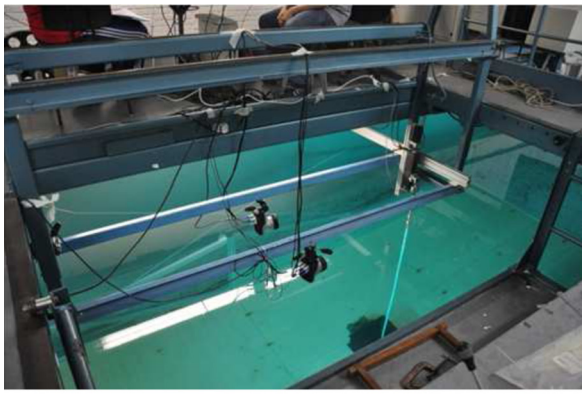

(a)

(b)

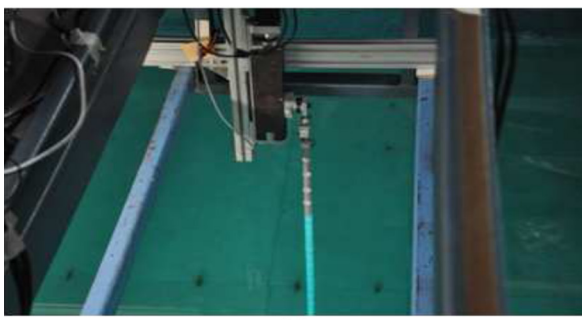

(c)

**Fig. 2 Pictures of the experimental arrangement. (*a*) General view of the experimental setup, (*b*) submerged cameras, and (*c*) servomotor device.**

modes $\psi_n(z)$ are here chosen to be simply represented by sinusoidal functions.

In fact and strictly speaking, sinusoidal functions represent the Eigen modes of a horizontal tensioned string. Section 4 focuses on the presentation of the modal analysis approach employed in the analytical model that supports the discussion of the experimental results.

## 4 Modal Analysis

As discussed in Sec. 3, sinusoidal functions are taken as a first and simple choice to represent the Eigen modes $\psi_n(z)$. In the present section, the focus is the procedure to obtain the time series $u_n^*(t) = u_n(t)/D$ that represents the oscillating amplitude of the $n$th-Eigen mode. For this, consider that, at a given instant, $t$, $x(z, t)$ represents the oscillatory part of the *elastica* of the model. The amplitude of the $n$-Eigen mode can be obtained by standard orthogonal projection, written as

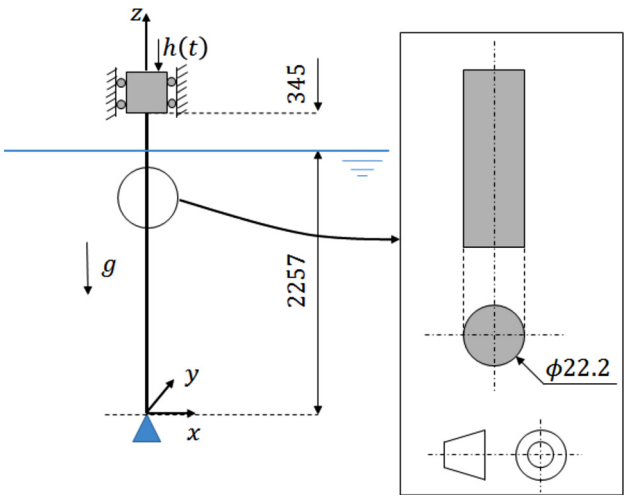


**Fig. 3 Sketch of the experimental setup**

$$u_n(t) = \frac{\langle x(z,t), \psi_n(z)\rangle}{\langle \psi_n(z), \psi_n(z)\rangle} = \frac{\int_0^L x(z,t)\psi_n(z,t)dz}{\int_0^L \psi_n^2(z,t)dz} \tag{3}$$

As an illustrative example of the use of the modal analysis proposed, Fig. 5 presents the original data at an instant $\bar{t}$ and its reconstruction considering the first four Eigen modes. This was found to recover the original data satisfactorily, for the purposes of the present analysis.

Notice that Eq. (3) allows to investigate the dynamics of the system by just considering a few Eigen modes, instead of the 43 time series of Cartesian coordinates. Table 3 presents the characteristic amplitude (obtained by computing the average of the 10% of the highest peaks, as in Ref. [18]) and the dominant frequency $f_d$ of the modal amplitude time series.

## 5 Analytical Model

In this analytical model, the bending stiffness is neglected when compared to the geometric stiffness. In fact, bending stiffness effect is relatively small, and, in the case of low numbered modes, confined only to the cylinder extremities, see Refs. [1] and [19]. However, this effect could be considered, from a WKB approximation, as shown in Refs. [16] and [17], or, alternatively, by transforming the fourth-order differential equation into a second-order one, substituting the bending stiffness term with an

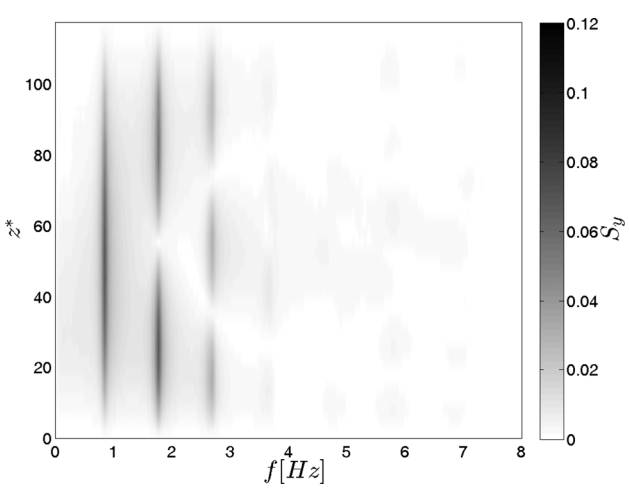


**Fig. 4 Spanwise distribution of PSD. Free decay tests in still water.**

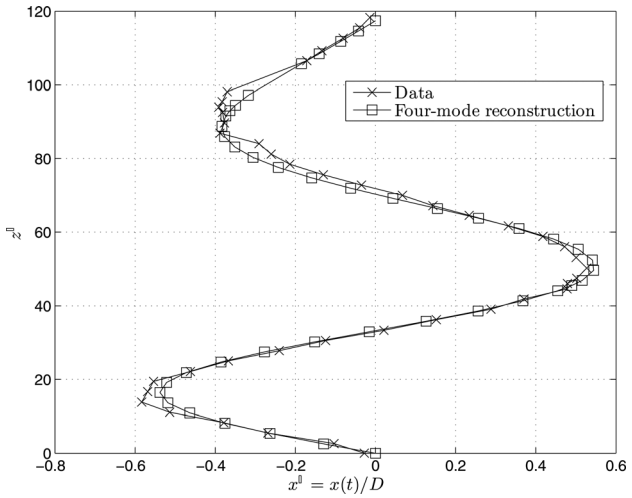


**Fig. 5 Example of reconstruction of the *elastica*. Original data and reconstruction with four modes: $f_t$:$f_{N,1}$ = 3:1.**

**Table 3 Characteristic amplitude and frequency of the modal amplitude time series**

| | $u_n^0/D$ | | | $f_d/f_{N,1}$ | | |
|---|---|---|---|---|---|---|
| $f_t$:$f_{N,1}$ | $n=1$ | $n=2$ | $n=3$ | $n=1$ | $n=2$ | $n=3$ |
| 1:3 | 0.10 | 0.05 | 0.04 | 1.00 | 0.33 | 0.33 |
| 1:1 | 0.38 | 0.18 | 0.10 | 1.00 | 1.00 | 2.00 |
| 2:1 | 0.63 | 0.45 | 0.16 | 1.00 | 2.00 | 2.00 |
| 3:1 | 0.05 | 0.12 | 0.45 | 3.00 | 3.00 | 3.00 |

additional and approximately equivalent geometric stiffness one; see Mazzilli et al. [20]. Following the simplest approach, the lateral displacement is given by the equation of a vertical string subjected to a nonlinear[3] damping term, in the form of the following equation:

$$m_t \frac{\partial^2 x(z,t)}{\partial t^2} + \frac{1}{2}\rho D C_D \frac{\partial x(z,t)}{\partial t}\left|\frac{\partial x(z,t)}{\partial t}\right| - \frac{\partial}{\partial z}\left(T(z,t)\frac{\partial x(z,t)}{\partial z}\right) = 0 \tag{4}$$

In the previous equation, $m_t = m_l + m_{ad}$ is the total mass per unit length (added mass $m_{ad}$ included), $C_D$ is the drag coefficient (supposed independent of the spanwise position) and $\rho$ is the fluid density. The total tension is $T(z, t) = T_t - \gamma(L - z) + T_d$, where $\gamma$ is the immersed weight per unit length (weight per unit length minus buoyancy contribution) and $T_d = (EA/L_0)A_t\cos(\omega_t t)$ is the dynamic tension induced by the top motion. Albeit it is well know that added mass and drag coefficients depend on the oscillation amplitude, in this paper these parameters will be considered constant and equal to 1 and 1.2, respectively.

Considering $x(z, t) = \psi_n(z)u_n(t)$ and by applying the Galerkin approach (multiplying Eq. (4) by $\psi_n(z) = \sin(n\pi(z/L))$ and integrating along the cylinders's length), the following modal oscillator equation is obtained:

$$M_n\ddot{u}_n + \beta_n|\dot{u}_n|\dot{u}_n + (\eta_n + \xi_n\cos(\omega_t t))u_n = 0 \tag{5}$$

where the modal parameters are given by

$$M_n = \int_0^L m_t\psi_n^2(z)dz = (m_l + m_{ad})\frac{L}{2} \tag{6}$$

$$\beta_n = \int_0^L \frac{1}{2}\rho C_D D|\psi_n(z)|\psi_n^2(z)dz \tag{7}$$

$$\eta_n = \int_0^L \frac{\partial}{\partial z}(T_t - \gamma(L-z)\psi_n'(z))\psi_n(z)dz = \left(\frac{n\pi}{2}\right)^2\left(2\frac{T_t}{L} - \gamma\right) \tag{8}$$

$$\xi_n = \left(\frac{n\pi}{2}\right)^2\left(\frac{EA}{L_o}\right)\frac{2A_t}{L} \tag{9}$$

Notice that $M_n$ and $\eta_n$ may be defined as the modal mass and stiffness, respectively, such that $\omega_{N,1} = \sqrt{\eta_1/M_1}$ is the theoretical value of the first Eigen frequency (in rad/s). Computing $\eta_1$ and $M_1$, we obtain $\omega_{N,1} = 5.24$ rad/s, which is, practically, the experimental result for the first Eigen frequency (i.e., $2\pi \times 0.84 = 5.28$ rad/s), as already presented. $\xi_n$ gives the modal stiffness modulation amplitude and $\beta_n$ is the nonlinear modal damping.

Aiming at obtaining a classical form of Mathieu's equation, Eq. (5) can be written considering the nondimensional time $2\tau = \omega_t t$, leading to the following equation:

$$\frac{d^2u_n(\tau)}{d\tau^2} + 2\mu_n\frac{du_n(\tau)}{d\tau}\left|\frac{du_n(\tau)}{d\tau}\right| + (\delta_n + 2\varepsilon_n\cos(2\tau))u_n(\tau) = 0 \tag{10}$$

where

$$\mu_n = \frac{\beta_n}{2M_n} \tag{11}$$

$$\delta_n = \frac{4\eta_n}{M_n\omega_t^2} \tag{12}$$

$$\varepsilon_n = \frac{2\xi_n}{M_n\omega_t^2} \tag{13}$$

It is important to highlight the differences between the alterative forms of Mathieu's equation, Eqs. (1) and (10). The differences, in form and consequently in the definition of the parameters, are related to the scaling of both, the nondimensional time and the parametric excitation amplitude.

The experimental data for $\delta_n$ and $\varepsilon_n$ are presented in Table 4. These values will be plotted onto the Strutt diagram for the first three Eigen modes.

Section 6 discusses the experimental results. This discussion is carried out focusing on the time series $x^*(z^*, t)$ plotted in scalograms, the spanwise distribution of corresponding PSD $S_x(z^*, f)$, and on results of modal decomposition analysis plotted onto Strutt diagrams. Such results are complemented with time series of modal amplitude and corresponding power spectra, as well as modal phase portraits.

## 6 Results and Discussion

Figure 6 presents the scalograms of the oscillatory component of $x^*(z^*, t)$ for a time interval of 10 s. Aiming at a better visualization, the color bars do not follow the same scale. Figure 7 presents the spanwise spectral distribution $S_x(z^*, f)$ computed from the whole acquisition time (120 s).

Considering the $f_t$:$f_{N,1}$ = 1:3 case, Fig. 6(*a*) indicates a standing wave pattern response. It can be noticed that the oscillations near the bottom are larger than those close to the top, as expected, since tension decreases with depth. This result is also observed in the $S_x(z^*, f)$ plot shown in Fig. 7(*a*), where subharmonic responses

[3]Notice that the only nonlinear term preserved in this mathematical model is that related to the hydrodynamic damping. Other nonlinear terms could be considered, as those related to stretching, see, e.g., Ref. [20].

**Table 4 Experimental points in the $\delta_n$–$\varepsilon_n$ plane**

| | $\delta_n$ | | | $\varepsilon_n$ | | |
|---|---|---|---|---|---|---|
| $n$ | 1 | 2 | 3 | 1 | 2 | 3 |
| 1:3 | 35.54 | 142.17 | 319.88 | 7.02 | 28.09 | 63.19 |
| 1:1 | **3.95** | 15.80 | 35.54 | **0.78** | 3.12 | 7.02 |
| 2:1 | **0.99** | **3.95** | 8.89 | **0.20** | **0.78** | 1.76 |
| 3:1 | 0.44 | 1.76 | **3.95** | 0.09 | 0.35 | **0.78** |

Bolded points are close to the transition curves or inside unstable regions.

clearly show up. In fact, the same plot also reveals other spectral components at $f$:$f_{N,1} = 1 \pm 1/3$.

The multicomponent character of the response is also observed in the $f_t$:$f_{N,1} = 1$:1 case, presented in Figs. 6(*b*) and 7(*b*). The $S_x(z^*, f)$ spectrum is mainly composed by two harmonics, at $f_{N,1}$ and $2f_{N,1}$. The scalogram indicates a marked presence of traveling waves, contrary to the $f_t$:$f_{N,1} = 1$:3 case. Furthermore, the celerity of the traveling waves, given by the inclination of each trace of the scalogram depends on the position $z^*$. This fact is not surprising, since the tension decreases with depth.

The scalogram corresponding to the $f_t$:$f_{N,1} = 2$:1 case is qualitatively distinct from the previous ones. It reveals an interesting dynamic pattern, where dominant responses at two modes clearly coexist, the first and the second one. A pitchfork-like figure may be seen forming at midspan, alternately reinforcing vibrations of both dominant modes, along the upper or the lower part of the cylinder. A clearer picture of such an interesting dynamic behavior may be formed by analyzing the corresponding modal phase portraits, presented at the end of this section. Still considering the $f_t$:$f_{N,1} = 2$:1 case, the spectrum $S_x(z^*, f)$ also reveals the components $f = f_{N,1}$ and $f = 2f_{N,1}$, but the higher amount of energy is not related to the frequency of the top motion.

Finally, the case $f_t$:$f_{N,1} = 3$:1 is also distinct from the others analyzed in this section. The $S_x(z^*, f)$ plot (see Fig. 7(*d*)) is monochromatic and narrow-banded centered at $f = 3f_{N,1} = f_t$, and the scalogram presented in Fig. 6(*d*) clearly reveals a stable and repetitive standing wave pattern in the third Eigen mode. Hence, for this condition of prescribed top motion, the response in mainly due to the external excitation.

Now, we change the focus to the analysis of the Mathieu instability by using the Strutt diagrams for the first, second, and third Eigen modes. The results of the Strutt diagram will be correlated with the scalograms and spectra presented in Figs. 6 and 7.

The Strutt diagrams for the first three Eigen modes are presented in Fig. 8. First, let us consider only the first Eigen mode (see Fig. 8(*a*)). From the mentioned figure, it is clearly visible that the green square is in an unstable region of the Strutt diagram. Hence, the top excitation frequency $f_t$:$f_{N,1} = 2$:1 leads to Mathieu instability for the first Eigen mode. It is worth to emphasize that, despite the combination of the values of the parameters $\delta$ and $\varepsilon$ leading to the unstable region, the amplitude of motion is relatively small. This fact is associated with the nonlinear damping and was already pointed out in Ref. [7]. Still considering the first Eigen mode, the red triangle, which corresponds to the $f_t$:$f_{N,1} = 1$:1 case, is at a transitional curve. Thus, in this case we can also expect oscillations with non-negligible amplitudes. Notice also that, as the amplitude of the parametric excitation is small, neither the $f_t$:$f_{N,1} = 2$:1 case or the $f_t$:$f_{N,1} = 1$:1 one are close to the secondary bifurcation curve. Such a curve is graphed in red and was constructed from Ref. [6], after rescaling from $\bar{\delta} - \bar{\varepsilon}$ to the $\delta$–$\varepsilon$ diagram.

The Strutt diagram for the second Eigen mode is shown in Fig. 8(*b*). Notice that, the $f_t$:$f_{N,1} = 2$:1 ($f_t$:$f_{N,2} = 1$:1) case is practically at a transition curve, such that Mathieu's instability might be expected. On the other hand, the points corresponding to the cases

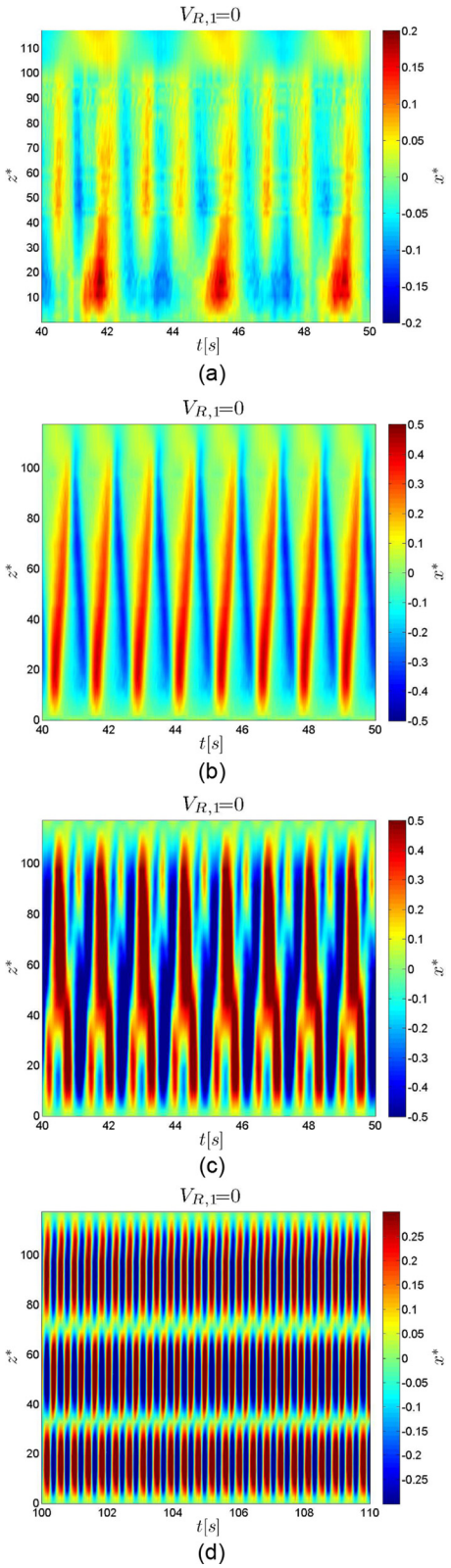


**Fig. 6 Scalograms $x^*(z^*, t)$. Only 10 s of acquisition are shown. (*a*) $f_t$:$f_{N,1}$ = 1:3, (*b*) $f_t$:$f_{N,1}$ = 1:1, (*c*) $f_t$:$f_{N,1}$ = 2:1, and (*d*) $f_t$:$f_{N,1}$ = 3:1.**

$f_t$:$f_{N,1} = 1$:1 and $f_t$:$f_{N,1} = 3$:1 are close enough to the transition to instability, such that any small perturbation in one of the parameters, as for instance in the added mass coefficient, might trigger Mathieu instability for the second Eigen mode, in this excitation frequency as well. This discussion agrees with the characteristic amplitude $u_2^0$ presented in Table 3, for which the higher value is

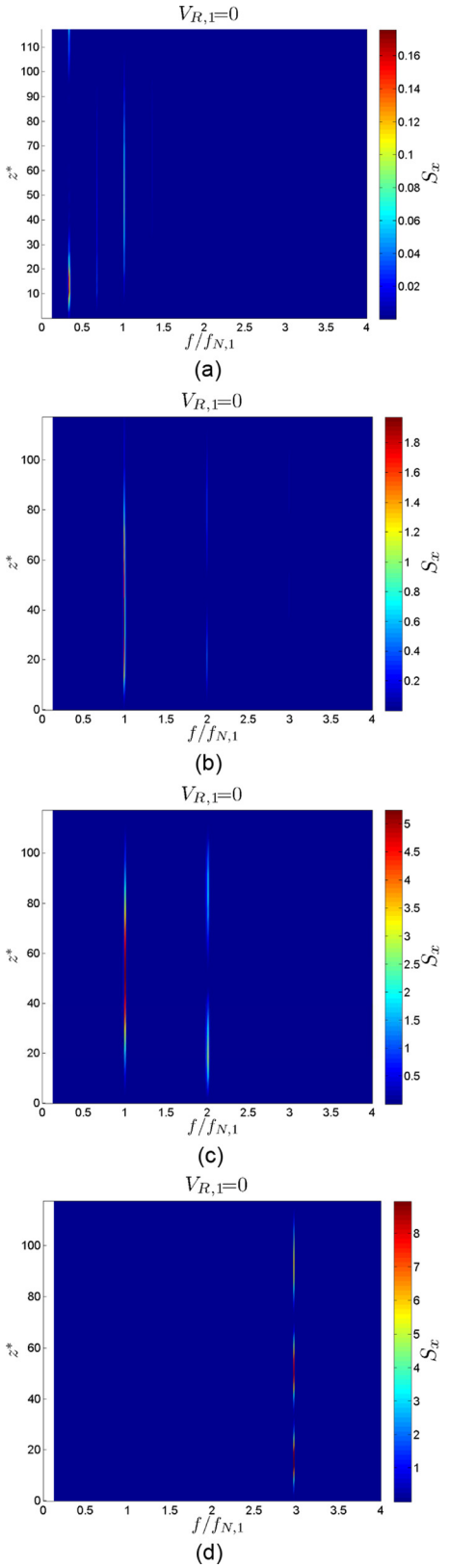


**Fig. 7 PSD spectra $S_x(z^*, f)$. (*a*) $f_t$:$f_{N,1}$ = 1:3, (*b*) $f_t$:$f_{N,1}$ = 1:1, (*c*) $f_t$:$f_{N,1}$ = 2:1, and (*d*) $f_t$:$f_{N,1}$ = 3:1.**

related to $f_t$:$f_{N,1} = 2$:1, but with non-negligible oscillations in the cases $f_t$:$f_{N,1} = 1$:1 and $f_t$:$f_{N,1} = 3$:1.

The Strutt diagram for the third Eigen mode is presented in Fig. 8(*c*). The latter plot indicates that the top excitation with frequency $f_t$:$f_{N,1} = 3$:1 leads to Mathieu instability. In the same plot, the

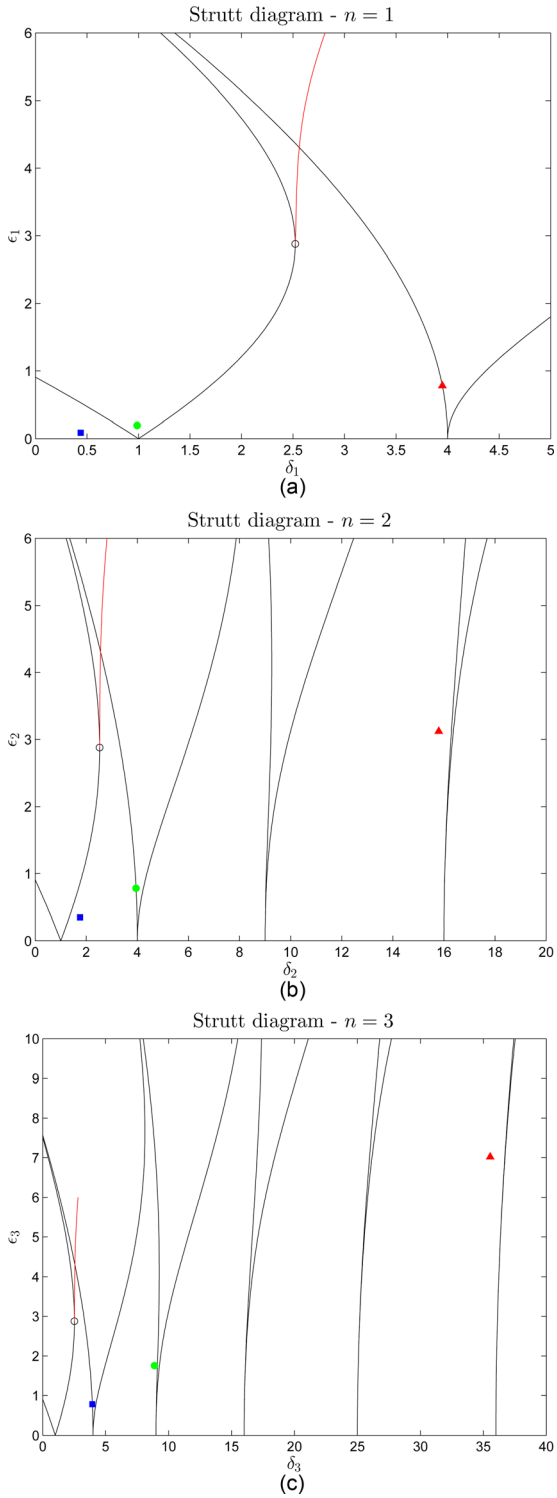


**Fig. 8 Strutt diagrams. Red (triangle): $f_t$:$f_{N,1}$ = 1:1; green (circle): $f_t$:$f_{N,1}$ = 2:1; blue (square): $f_t$:$f_{N,1}$ = 3:1. Results for the condition $f_t$:$f_{N,1}$ = 1:3 are within the stable region and are not shown. (*a*) First Eigen mode, (*b*) second Eigen mode, and (*c*) third Eigen mode.**

green square is located close to a transition curve. Once again, the results from Table 3 agree with those predicted by the Strutt diagram, with the higher amplitude $u_3^0/D$ being observed for the $f_t$:$f_{N,1} = 3$:1 case. Furthermore, it is observed the dominance of vibration of the third Eigen mode in the condition with top motion excitation at $f_t$:$f_{N,1} = 3$:1, as already discussed in the analysis of the scalograms and the PSD plots (see Figs. 6(*d*) and 7(*d*), respectively).

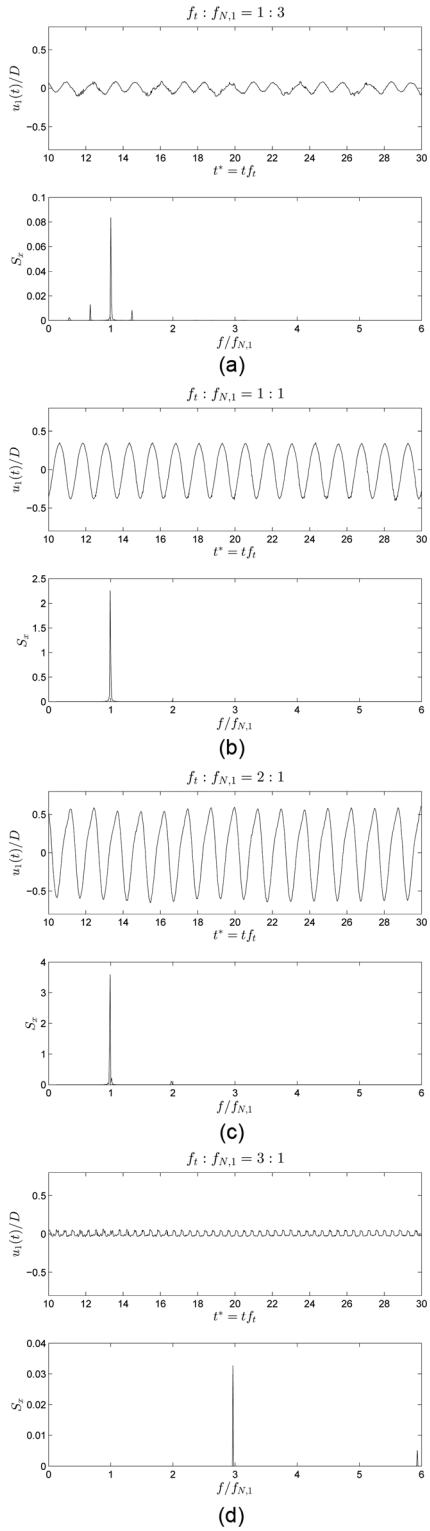


**Fig. 9 Modal amplitude time series $u_1(t)/D$ and corresponding PSD. (*a*) $f_t:f_{N,1} = 1:3$, (*b*) $f_t:f_{N,1} = 1:1$, (*c*) $f_t:f_{N,1} = 2:1$, and (*d*) $f_t:f_{N,1} = 3:1$.**

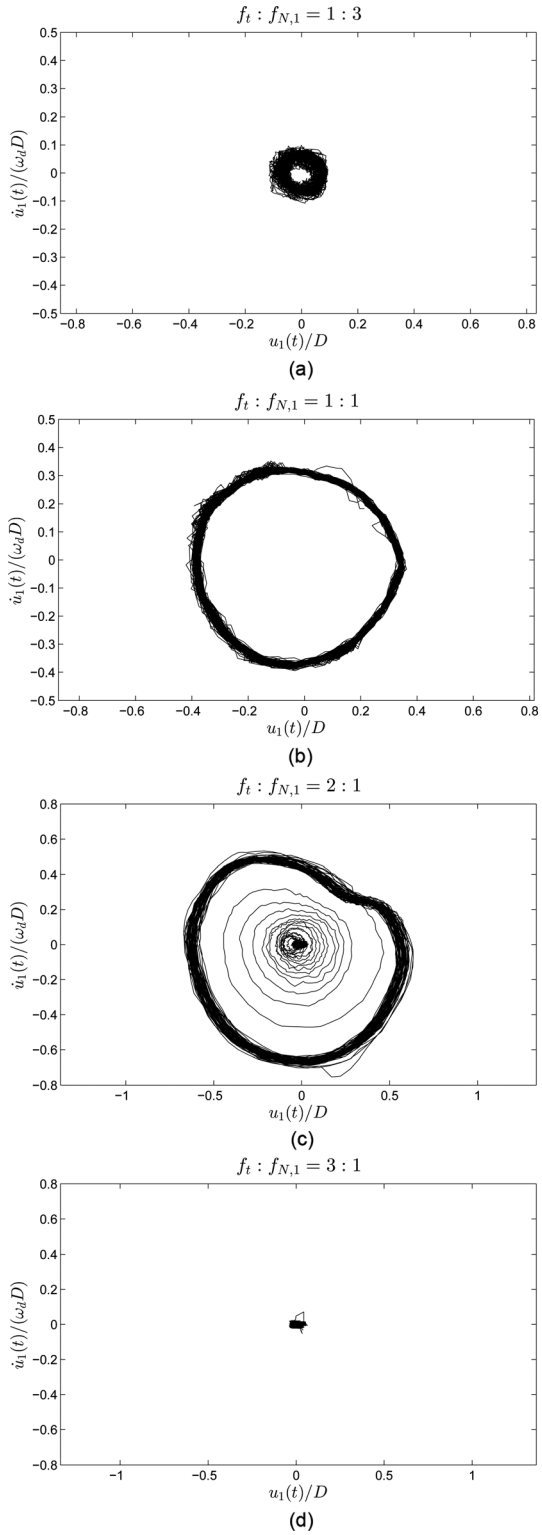


**Fig. 10 First mode phase portraits $\dot{u}_1/(\omega_d D)$ versus $u_1(t)/D$. (*a*) $f_t:f_{N,1} = 1:3$, (*b*) $f_t:f_{N,1} = 1:1$, (*c*) $f_t:f_{N,1} = 2:1$, and (*d*) $f_t:f_{N,1} = 3:1$.**

Up to this point, we discussed the Strutt diagram based on the modal amplitude time series for each of the chosen Eigen modes $\psi_n(z)$, $n = 1, 2, 3$. Now, we turn our attention to investigate Mathieu instabilities for each excitation frequency. This approach allows a straightforward way to interpret the scalograms and the PSD plots presented in Figs. 6 and 7.

The first case analyzed is that in which $f_t:f_{N,1} = 1:1$, marked as red triangles in Fig. 8. For this excitation condition, only the first Eigen mode is at a transition curve, hence subjected to significant oscillations. This fact is confirmed by modal amplitudes presented in Table 3.

Considering now the case with excitation frequency $f_t:f_{N,1} = 2:1$, the green squares in Fig. 8 indicate not only the Mathieu instability in the first Eigen mode (Fig. 8(*a*)) but also the possibility of this instability in the second and third Eigen modes (Figs. 8(*b*) and 8(*c*), respectively). These results may

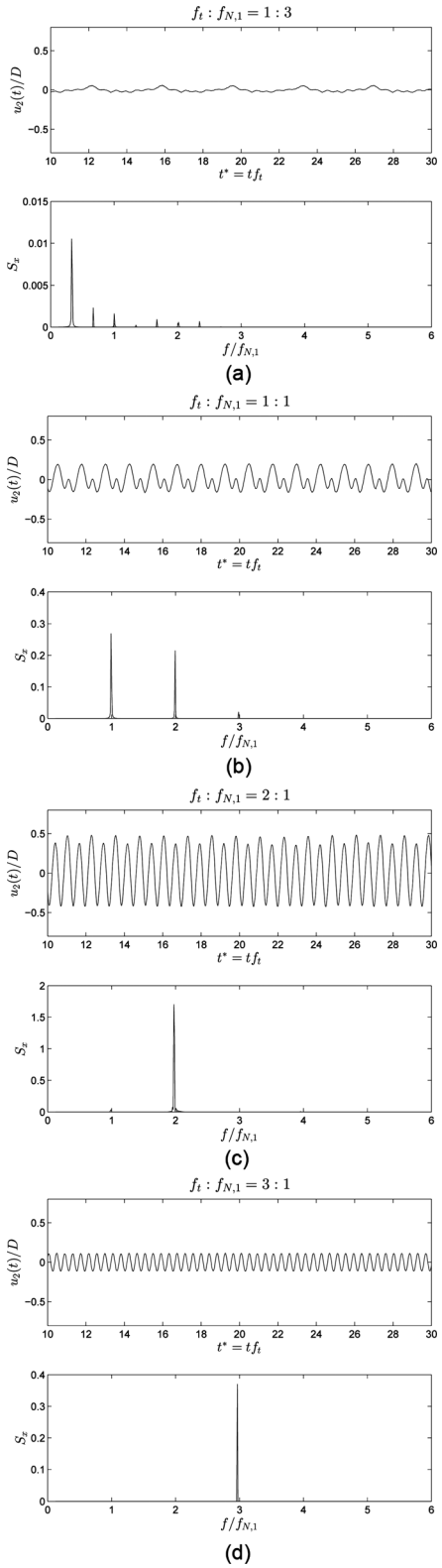


**Fig. 11 Modal amplitude time series $u_2(t)/D$ and corresponding PSD. (*a*) $f_t$:$f_{N,1}$ = 1:3, (*b*) $f_t$:$f_{N,1}$ = 1:1, (*c*) $f_t$:$f_{N,1}$ = 2:1, and (*d*) $f_t$:$f_{N,1}$ = 3:1.**

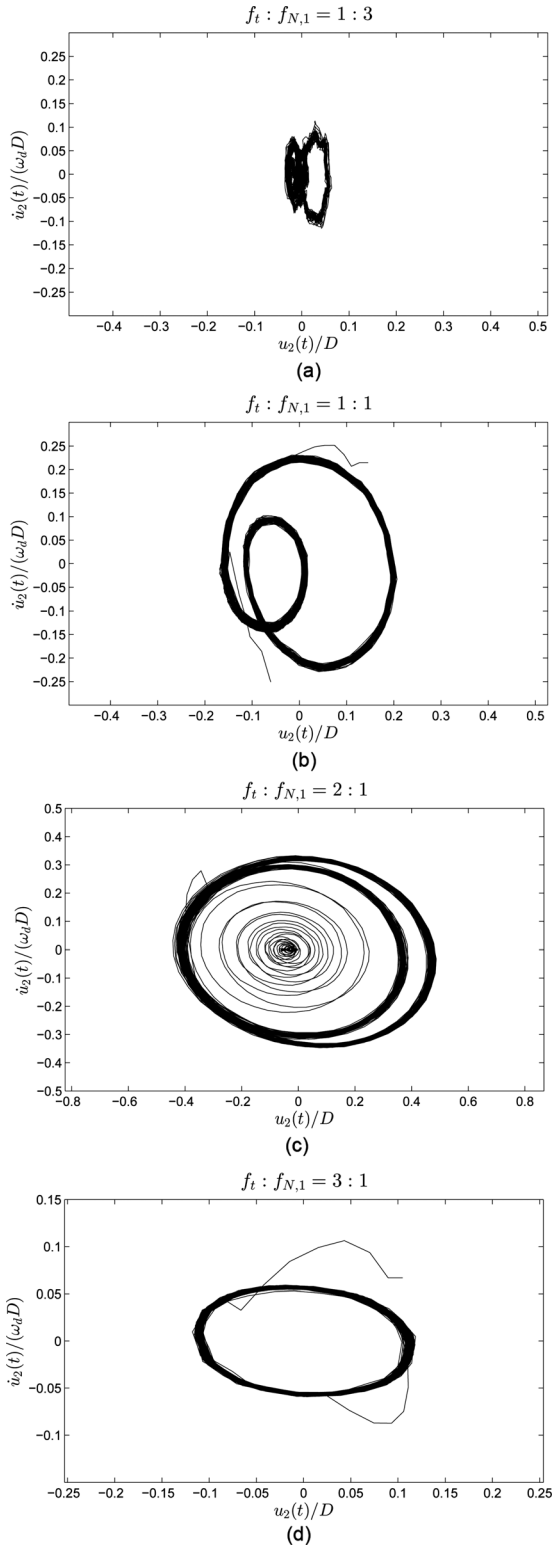


**Fig. 12 Second mode phase portraits $\dot{u}_2/(\omega_d D)$ versus $u_2(t)/D$. (*a*) $f_t$:$f_{N,1}$ = 1:3, (*b*) $f_t$:$f_{N,1}$ = 1:1, (*c*) $f_t$:$f_{N,1}$ = 2:1, and (*d*) $f_t$:$f_{N,1}$ = 3:1.**

justify the modal amplitude distribution presented in Table 3. Moreover, the composition of modes may be related to the alternating "fork" pattern verified in the scalogram shown in Fig. 6(*b*).

Finally, in the case with $f_t$:$f_{N,1} = 3$:1, the blue square in Fig. 8(*c*) reveals that the third Eigen mode is at a transition curve, whereas for the others cases, the referred marker is inside stable regions. This result totally agrees with the character of both the corresponding scalogram and spanwise PSD plots shown, respectively, in Figs. 6(*d*) and 7(*d*), as well as with the characteristic oscillation amplitude $u_3^0$ results presented in Table 3. The last set of results that will be discussed is the modal amplitude time series and the corresponding PSD plots. These results are shown in Figs. 9–14. Considering the first mode amplitude time series $u_1$ (Fig. 9), it is

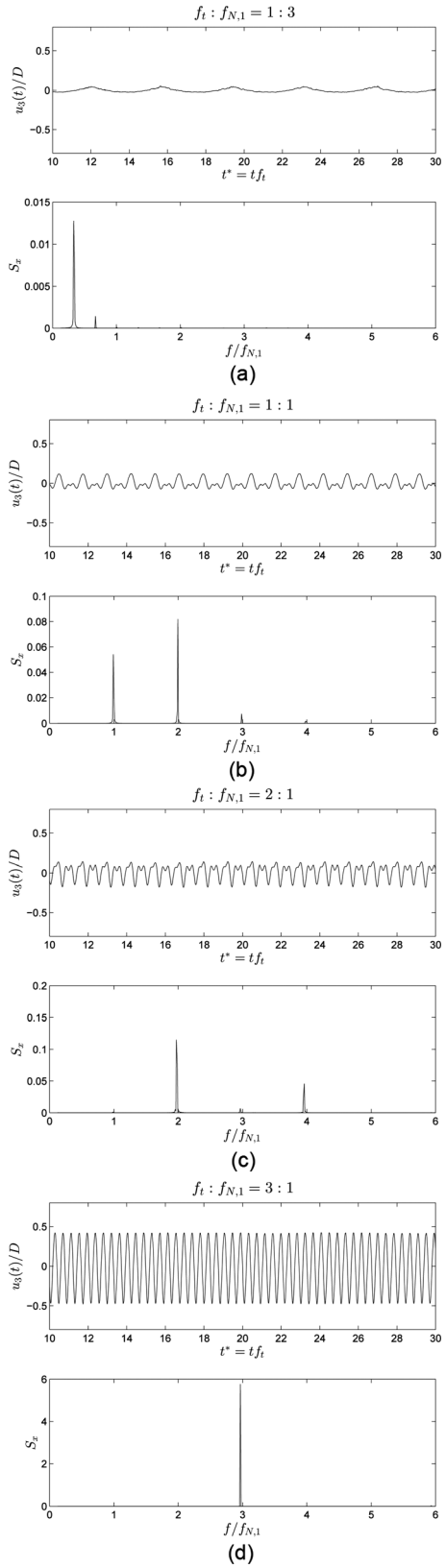


**Fig. 13 Modal amplitude time series $u_3(t)/D$ and corresponding PSD. (*a*) $f_t$:$f_{N,1}$ = 1:3, (*b*) $f_t$:$f_{N,1}$ = 1:1, (*c*) $f_t$:$f_{N,1}$ = 2:1, and (*d*) $f_t$:$f_{N,1}$ = 3:1.**

clearly visible that the dominant oscillation frequency is $f/f_{N,1} = 1$ for the $f_t$:$f_{N,1}$ = 1:1 and 2:1 cases. The oscillation amplitude for the 3:1 case is almost negligible. The corresponding phase portraits (see Fig. 10) indicate a well defined periodic behavior of these

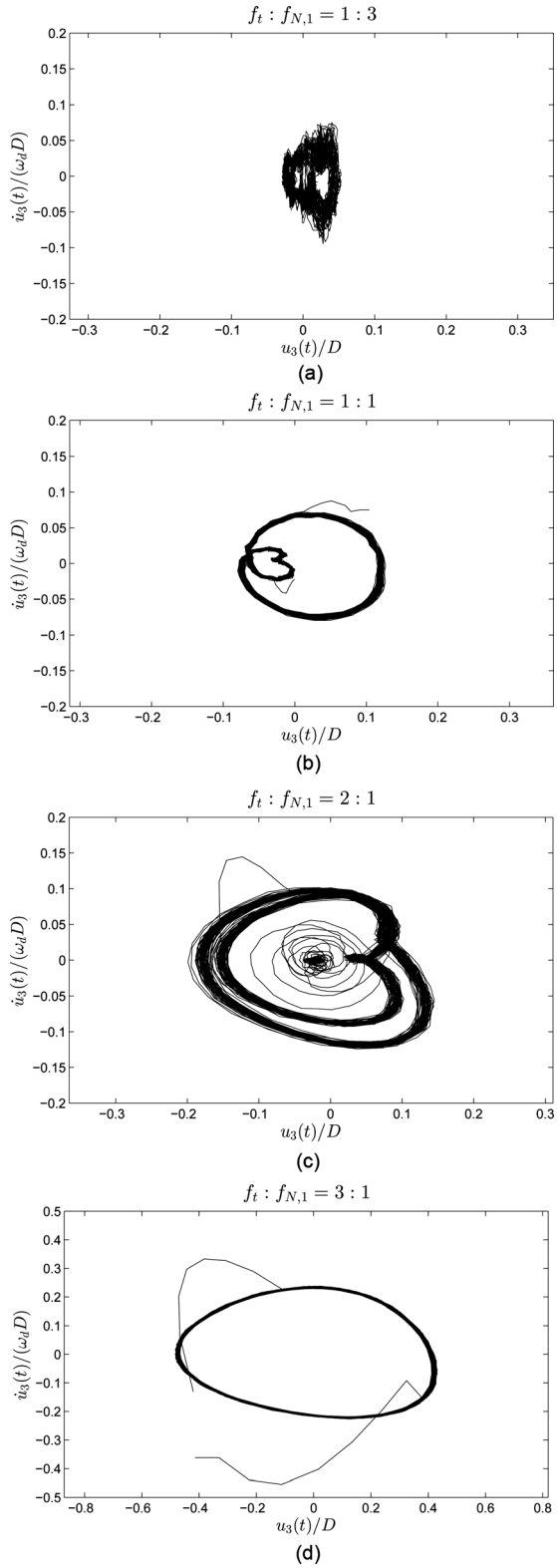


**Fig. 14 Third mode phase portraits $\dot{u}_3/(\omega_d D)$ versus $u_3(t)/D$. (*a*) $f_t$:$f_{N,1}$ = 1:3, (*b*) $f_t$:$f_{N,1}$ = 1:1, (*c*) $f_t$:$f_{N,1}$ = 2:1, and (*d*) $f_t$:$f_{N,1}$ = 3:1.**

time series. On the other hand, the response of the 1:3 case is dominated by the first Eigen frequency, but also presents energy at components $f/f_{N,1} = 1 + 1/3$ (sum frequency) and $f/f_{N,1} = 1 - 1/3$ (difference frequency). The presence of sum and difference frequencies was already pointed out in experimental results of simultaneous VIV phenomenon and parametric excitation of a semi-immersed flexible cylinder (see Ref. [21]).

**Table 5 Frequency ratios of periodic response. Prediction by Strutt diagram versus determined from spectral analysis.**

| | | | $f_R:f_{N,1}$ | | $f_R:f_t$ | | $f_R:f_{N,n}$ | |
|---|---|---|---|---|---|---|---|---|
| $n$ | $f_t:f_{N,1}$ | $f_t:f_{N,n}$ | Strutt | Spectral | Strutt | Spectral | Strutt | Spectral |
| 1 | 1:1 | 1:1 | 1:1 | 1:1 | 1:1 | 1:1 | 1:1 | 1:1 |
| | 2:1 | 2:1 | 1:1 | 1:1 | 1:2 | 1:2 | 1:1 | 1:1 |
| | 3:1 | 3:1 | — | 3:1* | — | 1:1* | — | 3:1* |
| 2 | 1:1 | 1:2 | — | 1:1, 2:1 | — | 1:1, 2:1 | — | 1:2, 1:1 |
| | 2:1 | 2:2 | 2:1 | 2:1 | 1:1 | 1:1 | 1:1 | 1:1 |
| | 3:1 | 3:2 | — | 3:1* | — | 3:3* | — | 3:2* |
| 3 | 1:1 | 1:3 | — | 1:1, 2:1 | — | 1:1, 2:1 | — | 1:3, 2:3 |
| | 2:1 | 2:3 | — | 2:1, 4:1 | — | 1:1, 2:1 | — | 2:3, 4:3 |
| | 3:1 | 3:3 | 3:1 | 3:1 | 1:1 | 1:1 | 1:1 | 1:2 |

The symbol "—" indicates stability of the trivial solution $u_n = 0$. $f_R$ refers to the spectral components present in the response. * indicates negligible amplitudes—see, for example, Fig. 9(*d*).

Focusing now on the $u_2$ times series, the dynamic behavior is certainly more intricate, as can bee seen in Figs. 10 and 11. In the $f_t:f_{N,1} = 1:1$ case, the PSD analysis reveals oscillations with components $f/f_{N,1} = 1$ and $f/f_{N,1} = 2$. Hence, the model vibrates with the shape of the second Eigen mode and at the first Eigen frequency. This might be attributed to modeling an intrinsically nonlinear structure and related phenomena by employing linear modes. Ongoing researches on this subject make use of nonlinear modes, which carry richer information on oscillation frequencies, amplitudes, and velocities, as an alternative analytical approach for this problem. The reader interested in theoretical discussion and applications of nonlinear modes is referred to Shawn and Pierre [22,23].

A summary of the above discussion can be found in Table 5, in which the frequency ratios of periodic responses predicted by the Strutt diagram are compared to those experimentally obtained from modal analysis. Recall that, in the usual Strutt diagram, the transitional curves which bound the instability regions are the loci of periodic solutions, alternating between $2T$ and $T$ periodic ones, as successive tongues of instability are considered; the first one, with vertex at $\delta = 1$, is $2T$. If damping is included, the transitional boundaries change to bifurcation lines, delimiting regions were periodic oscillations may appear. Comparing the predictions given by the plots in the Strutt diagrams with the experimental results obtained through the spectral analysis, a fair agreement is indeed obtained. For example, a Mathieu like instability, with a $2T$ periodic solution ($f_R:f_t = 1:2$), is clearly confirmed for the first Eigen mode; see Table 5, second line, $n = 1$. For the same Eigen mode, a $1T$ periodic solution ($f_R:f_t = 1:1$) shows up too (first line, $n = 1$). Similarly, $1T$ periodic solutions ($f_R:f_t = 1:1$) appear for the second (second line, $n = 2$) and for the third (third line, $n = 3$) Eigen modes.

On the other hand, the $2T$ periodic oscillation that might be expected for the third Eigen mode (second line, $n = 3$), since the corresponding plot in the Strutt diagram (Fig. 8(*c*)) is very close to the left boundary of the third instability tongue, is not confirmed by the spectral analysis. As a matter of fact, whenever the Strutt diagram does not clearly predict a single periodic solution for a given mode (what is marked with a horizontal trace in Table 5), the spectral analysis reveals a multifrequency response in that mode. In other words, periodic solutions emerging from Mathieu-like instabilities in a given mode appear to dominate other possible harmonic components, possibly presented in the same mode.

Before the final remarks, a last aspect should be highlighted. The use of sinusoidal functions as a projection set showed to be a good choice, balancing simplicity, and quality of results. Further investigations may take into account other set of functions in the Galerkin's projection scheme, by using more sophisticated approximations to the Eigen modes, as Bessel's or WKB asymptotics. However, other issues, as orthogonality properties, should be properly worked out.

## 7 Conclusions

Combining modal and spectral analysis with Mathieu instability modeling, an experimental investigation was carried out with a flexible and vertically immersed cylinder, subjected to harmonic vertical top motions. The dynamic response for distinct excitation frequency ratios, with respect to the first natural frequency, was analyzed and discussed.

In the frequency ratio case $f_t:f_{N,1} = 1:1$, the response amplitude scalogram indicated the presence of a traveling-wave pattern and the PSD plot $S_x(z^*, f)$ highlighted the predominance of the first two Eigen modes in the response. In the $f_t:f_{N,1} = 2:1$ case, the $S_x(z^*, f)$ also indicated the predominance of the first and second Eigen modes, but the scalogram revealed an alternating "fork pattern." The higher excitation frequency ratio tested corresponds to $f_t:f_{N,1} = 3:1$. Contrary to the previous ones, the latter condition was characterized by the predominance of a standing-wave pattern with the shape of the third Eigen mode.

In the case in which $f_t:f_{N,1} = 1:1$, the Strutt diagram pointed out the Mathieu instability in the first Eigen mode. On the other hand, for the case $f_t:f_{N,1} = 2:1$, the analysis of the Strutt diagram allowed to assert that the Mathieu instability may occur in more than one Eigen mode. This fact was verified through spectral analysis of the modal components time series.

Another interesting finding is that, whenever the Strutt diagram did not clearly predict a single periodic solution for a given mode, the spectral analysis revealed a multifrequency response in that mode. In other words, periodic solutions emerging from Mathieu-like instabilities appear to dominate other possible harmonic components in a given mode. These findings may contribute to the understanding of the dynamics of top tension risers or TLP tethers.

Further work on vertical cylinder dynamics shall address the analysis of experimental results of concomitant VIV and parametrically excited vibrations, already obtained during the same research project. Other aspects to be investigated include a multimode projection scheme as a way to verify the influence of the modal interactions in the response. Sensitiveness studies concerning the effect of added mass and drag coefficients on Mathieu instabilities are also interesting issues to be further considered.

## Acknowledgment

This work has been carried out after a research project sponsored by Petrobras, focusing in nonlinear dynamics of risers. The first author acknowledges FAPESP for his postdoctoral scholarship, Process No. 2013/09802-2. The second and third authors acknowledge CNPq, for the research Grant No. 30.3838/2008-6 and the Graduate Scholarship No. 131549/2013-8. Special thanks to the IPT technical staff for helping with the experiments.

## References

[1] Pesce, C. P., and Martins, C. A., 2005, "Numerical Computation of Riser Dynamics," *Numerical Modeling in Fluid–Structure Interaction*, S. Chakrabarti, ed., WIT Press, Southampton, UK, pp. 253–309.
[2] Silveira, L. M. Y., Martins, C. A., Cunha, L. D., and Pesce, C. P., 2007, "An Investigation on the Effect of Tension Variation on VIV of Risers," ASME Paper No. OMAE2007-29247.
[3] Joseffson, P. M., and Dalton, C., 2010, "An Analytical/Computational Approach in Assessing Vortex-Induced Vibration of a Variable Tension Riser," ASME J. Offshore Mech. Arct. Eng., **132**(3), p. 031302.
[4] Srinil, N., 2011, "Analysis and Prediction of Vortex-Induced Vibrations of a Variable-Tension Vertical Risers in Linearly Sheared Currents," Appl. Ocean Res., **33**(1), pp. 41–53.
[5] Meirovitch, L., 2003, *Methods of Analytical Dynamics*, Dover Publications, Mineola, NY.
[6] Ramani, D. V., Keith, W. L., and Rand, R. H., 2004, "Perturbation Solution for Secondary Bifurcation in the Quadratically-Damped Mathieu Equation," Int. J. Non-Linear Mech., **39**(3), pp. 491–502.

[7] Patel, M. H., and Park, H. I., 1991, "Dynamics of Tension Leg Platform Tethers at Low Tension. Part I—Mathieu Stability at Large Parameters," Mar. Struct., **4**(3), pp. 257–273.
[8] Simos, A. N., and Pesce, C. P., 1997, "Mathieu Stability in the Dynamics of TLP's Tethers Considering Variable Tension Along the Length," *Offshore Engineering*, F. L. L. B. Carneiro, A. J. Ferrante, R. C. Batista, and N. F. F. Ebecken, eds., WIT Press, Ashurst, UK.
[9] Chatjigeorgiou, I. K., and Mavrakos, S. A., 2002, "Bounded and Unbounded Coupled Transverse Response of Parametrically Excited Vertical Marine Risers and Tensioned Cable Legs for Marine Applications," Appl. Ocean Res., **24**(6), pp. 341–354.
[10] Zeng, X., Xu, W., Li, X., and Wu, Y., 2008, "Nonlinear Dynamic Responses of the Tensioned Tether Under Parametric Excitation," Eighteenth International Offshore and Polar Engineering Conference (ISOPE 2008), Vancouver, Canada, July 6–11, pp. 78–83.
[11] Yang, H., Xiao, F., and Xu, P., 2013, "Parametric Instability Prediction in a Top-Tensioned Riser in Irregular Waves," Ocean Eng., **70**, pp. 39–50.
[12] Rateiro, F., Pesce, C. P., Gonçalves, R. T., Franzini, G. R., Fujarra, A. L. C., Salles, R., and Mendes, P., 2012, "Risers Model Tests: Scaling Methodology and Dynamic Similarity," 22nd International Ocean and Polar Engineering Conference (ISOPE 2012), Rhodes, Greece, June 17–22, pp. 439–445.
[13] Rateiro, F., Gonçalves, R. T., Pesce, C. P., Fujarra, A. L. C., Franzini, G. R., and Mendes, P., 2013, "A Model Scale Experimental Investigation on Vortex-Self Induced Vibrations (VSIV) of Catenary Risers," ASME Paper No. OMAE2013-10447.
[14] Franzini, G. R., Rateiro, F., Gonçalves, R. T., Pesce, C. P., and Mazzilli, C. E. N., 2012, "An Experimental Assessment of Rigidity Parameters of a Small-Scaled Riser Model," 12th Pan American Congress of Applied Mechanics (PACAM XII), St. Augustine, Trinidad, Jan. 2–6.
[15] de Mello, P. C., Rateiro, F., Fujarra, A. L. C., Oshiro, A. T., Neves, C. R., dos Santos, M. F., and Tannuri, E. A., 2011, "Experimental Set-Up for Analysis of Subsea Equipment Installation," ASME Paper No. OMAE2011-49946.
[16] Pesce, C. P., Fujarra, A. L. C., Simos, A. N., and Tannuri, E. A., 1999, "Analytical and Closed Form Solutions for Deep Water Riser-Like Eigenvalue Problem," Ninth International Offshore and Polar Engineering Conference (ISOPE), Brest, France, May 30–June 4, pp. 255–264.
[17] Chatjigeorgiou, I. K., 2008, "Application of the WKB Method to Catenary-Shaped Slender Structures," Math. Comput. Modell., **48**(1–2), pp. 249–257.
[18] Franzini, G. R., Gonçalves, R. T., Meneghini, J. R., and Fujarra, A. L. C., 2013, "One and Two Degrees-of-Degrees Vortex-Induced Vibration Experiments With Yawed Cylinders," J. Fluids Struct., **42**, pp. 401–420.
[19] Chatjigeorgiou, I. K., 2008, "Solution of the Boundary Layer Problem for Calculating the Natural Modes of Riser-Type Slender Structures," ASME J. Offshore Mech. Arct. Eng., **130**(1), p. 011003.
[20] Mazzilli, C. E. N., Lenci, S., and Demeio, L., 2014, "Non-Linear Free Vibrations of Tensioned Vertical Risers," 8th European Nonlinear Dynamics Conference (ENOC2014), Vienna, Austria, July 6–11.
[21] Franzini, G. R., Gonçalves, R. T., Pesce, C. P., Fujarra, A. L. C., Mazzilli, C. E. N., Meneghini, J. R., and Mendes, P., 2014, "Vortex-Induced Vibration Experiments With a Long Semi-Immersed Flexible Cylinder Under Tension Modulation: Fourier Transform and Hilbert–Huang Spectral Analyses," J. Braz. Soc. Mech. Sci. Eng. (online).
[22] Shaw, S. W., and Pierre, C., 1991, "Non-Linear Normal Modes and Invariant Manifolds," J. Sound Vib., **150**(1), pp. 170–173.
[23] Shaw, S. W., and Pierre, C., 1993, "Normal Modes for Non-Linear Vibratory Systems," J. Sound Vib., **164**(1), pp. 85–124.